

This is the accepted manuscript made available via CHORUS. The article has been published as:

Structural and ferroelectric phase evolution in  
 $[\text{KNbO}_3]_{1-x}[\text{BaNi}_{1/2}\text{Nb}_{1/2}\text{O}_{3-\delta}]_x$   
( $x=0,0.1$ )

Christopher J. Hawley, Liyan Wu, Geoffrey Xiao, Ilya Grinberg, Andrew M. Rappe, Peter K. Davies, and Jonathan E. Spanier

Phys. Rev. B **96**, 054117 — Published 28 August 2017

DOI: [10.1103/PhysRevB.96.054117](https://doi.org/10.1103/PhysRevB.96.054117)

1 **Structural and ferroelectric phase evolution in  $[\text{KNbO}_3]_{1-x}[\text{BaNi}_{1/2}\text{Nb}_{1/2}\text{O}_{3-\delta}]_x$**   
2  **$(x = 0, 0.1)$**

3 C. J. Hawley,<sup>1</sup> L. Wu,<sup>2</sup> G. Xiao,<sup>1</sup> I. Grinberg,<sup>3</sup> A. M. Rappe,<sup>2,4</sup> P. K. Davies,<sup>2</sup> and J. E. Spanier<sup>1,5,\*</sup>

4 <sup>1</sup>*Department of Materials Science & Engineering,*  
5 *Drexel University, Philadelphia, PA 19104, USA*

6 <sup>2</sup>*Department of Materials Science & Engineering,*  
7 *University of Pennsylvania, Philadelphia, PA 19104, USA*

8 <sup>3</sup>*Department of Chemistry, Bar Ilan University, Ramat-Gan, 5290002, Israel*

9 <sup>4</sup>*Department of Chemistry, University of Pennsylvania, Philadelphia, PA 19104, USA*

10 <sup>5</sup>*Department of Physics, Drexel University, Philadelphia, PA 19104, USA*

11 (Dated: August 9, 2017)

The phase transition evolution for  $[\text{KNbO}_3]_{1-x}[\text{BaNi}_{1/2}\text{Nb}_{1/2}\text{O}_{3-\delta}]_x$  ( $x=0, 0.1$ ) is determined via complementary dielectric permittivity and Raman scattering measurements. Raman scattering by optical phonons over the range of 100-1000  $\text{cm}^{-1}$  for  $83 \text{ K} < T < 873 \text{ K}$  reveals six discernible zone-center optical phonon modes. Mode behaviors are observed through structural and ferroelectric phases in the solid solution  $x = 0.1$  and compared with those for end member  $x = 0$  and with the results of temperature-dependent dielectric permittivity. Rigorous peak fitting analyses of spectra collected from the solid solution and end member indicate structural and ferroelectric phase transition temperatures that are close to those for the  $\text{KNbO}_3$  end member despite the inclusion of 5 atomic % of ferroelectrically inactive Ni cations. Density functional theory calculations were performed in the solid solution and end member using both cation displacement and Berry phase-based methods. Differences in the electronic and polar properties between the solid solution and the end member highlights local and non-local characteristics, which are discussed in relation to the experimental data.

## I. INTRODUCTION

13 Ferroelectrics have long been recognized as an interesting alternative to conventional semiconductor junctions for  
 14 photo-excited carrier separation and photovoltaic solar energy conversion<sup>1-18</sup>, exhibiting the bulk photovoltaic (PV)  
 15 effect<sup>19-22</sup> and other ferroelectric polarization-induced or polarization-influenced carrier separation mechanisms, in-  
 16 cluding those due to domain walls and Schottky barriers. The design and realization of visible wavelength-absorbing  
 17 ferroelectric oxide perovskites poses special challenges for practical photovoltaic solar energy conversion due to the  
 18 inherently large band gap ( $\gtrsim 2.7$  eV) associated typically with an O  $2p$  valence and a transition metal  $d$  con-  
 19 duction band. Inclusion of other  $B$ -site cations (*e.g.*, Pd, Pt, etc.), substitutionally, within  $\text{PbTiO}_3$ <sup>23</sup> has been  
 20 proposed as a strategy for band gap lowering<sup>24-27</sup>. Introduction of Ni onto  $B$ -site  $\text{KNbO}_3$  in the solid solution  
 21  $[\text{KNbO}_3]_{1-x}[\text{BaNi}_{1/2}\text{Nb}_{1/2}\text{O}_{3-\delta}]_x$  ( $x = 0.1$ ) (KBNNO) was shown to result in significant decrease in band gap with-  
 22 out loss of ferroelectric ordering<sup>10</sup>, and relatively large shift currents in KBNNO (compared with  $\text{BiFeO}_3$ ) have been  
 23 predicted<sup>28</sup>. Recently, room-temperature Raman scattering spectra in bulk ceramic KBNNO have been reported<sup>29</sup>  
 24 for several different values of  $x$ .

25 Incorporation of ferroelectrically inactive cations can be accomplished without complete suppression of ferroelec-  
 26 tricity. However, concomitant decreases in ferroelectric phase transition temperature,  $T_c$ , with inactive cation con-  
 27 centration can be expected in accordance with well-known systems, *e.g.* Zr in  $\text{PbTiO}_3$  (PZT)<sup>30</sup>, and Sr in  $\text{BaTiO}_3$   
 28 forming the well-known incipient ferroelectric solid solution  $\text{Ba}_{1-x}\text{Sr}_x\text{TiO}_3$  (BST)<sup>31</sup>. Raman scattering spectroscopy  
 29 is effective for probing the onset of a phase transition with local correlation lengths as short as several unit cells. The  
 30 structural evolution and determination of  $T_c$  in  $\text{KNbO}_3$  and related  $A$ -site ( $A = \text{Na}, \text{Li}, \text{La}$ ) solid solutions  $\text{ANbO}_3$   
 31 (KNNO and KLNO) has been reported via temperature-dependent dielectric, Raman scattering, and infrared spec-  
 32 troscopic analyses<sup>32-40</sup>. Other studies of  $T_c$  evolution in doped  $\text{KNbO}_3$  have also been reported<sup>41-45</sup>. Unlike systems  
 33 that involve isovalent substitutions, such as PZT, BST, KNNO,  $\text{KTa}_{1-x}\text{Nb}_x\text{O}_3$ , and  $\text{K}_{1-x}\text{Li}_x\text{NbO}_3$ , the aliovalent  
 34 substitution of  $\text{Ni}^{2+}$  onto the  $B$ -site of  $\text{KNbO}_3$  is accompanied by formation of a neighboring O vacancy, producing  
 35 localized tensile strain near the cation-vacancy pair. Ferroelectric phase stability is a key consideration for potential  
 36 optoelectronic applications including PV solar energy conversion, making it important to consider the extent to which  
 37 the substitutional incorporation of Ni cations influences the structural and ferroelectric phase stability in the solid  
 38 solution KBNNO.

39 As summarized in Tables I and II, end member  $\text{KNbO}_3$  possesses fifteen modes, including three acoustic and twelve  
 40 optical phonons. Of the optical phonons, by symmetry,  $3 A_1 + 4 E$  are first-order Raman-active in the rhombohedral  
 41 ( $R3m$  or  $C_{3v}^5$ ) phase with an  $A_2$  phonon mode as Raman silent,  $4 A_1 + A_2 + 4 B_1 + 3 B_2$  in the orthorhombic ( $Amm2$   
 42 or  $C_{2v}^{14}$ ) phase, and  $3 A_1 + B_1 + 4 E$  in the tetragonal ( $P4mm$  or  $C_{4v}^1$ ) phase. First-order Raman scattering of the  
 43  $3 F_{1u} + F_{2u}$  modes is forbidden in the centrosymmetric cubic ( $Pm3m$  or  $O_h^1$ ) phase. Atomic site disorder lowers  
 44 translational symmetry, effectively relaxing Raman selection rules. This increases phonon scattering rates, manifesting  
 45 as broadened lineshapes, complicating determination of peak positions and mode assignments<sup>42-44,46</sup>. Nevertheless,  
 46 Raman-active mode assignments and transition temperatures in solid solutions such as (K,A) $\text{NbO}_3$  have been made  
 47 and can also be accomplished in  $B$ -site solid solution systems, based on comparison with end members. Here, we  
 48 report temperature-dependent dielectric response in bulk ceramic  $\text{KNbO}_3$  and KBNNO. Using rigorous lineshape and  
 49 peak fitting analyses, we show temperature-dependent evolution of the structural and ferroelectric phases in bulk  
 50 ceramic KBNNO from  $100\text{-}1000\text{ cm}^{-1}$  for  $83\text{ K} < T < 873\text{ K}$ , comparing our results with bulk ceramic  $\text{KNbO}_3$ .  
 51 Finally, we present the results of density functional theoretical analysis, calculating the structural relaxation and  
 52 electric polarization and theoretically estimating the  $T_c$  in order to compare with our experimental data.

## II. EXPERIMENTAL METHODS

54 Samples of  $[\text{KNbO}_3]_{1-x}[\text{BaNi}_{1/2}\text{Nb}_{1/2}\text{O}_{3-\delta}]_x$  ( $x = 0$  and  $0.1$ ) are synthesized by standard solid-state reaction  
 55 followed by a sintering process. High purity powders, including  $\text{K}_2\text{CO}_3$  (J.T. Baker, 99.9%),  $\text{BaCO}_3$  (Cerac, 99.9%),  
 56  $\text{Nb}_2\text{O}_5$  (Cerac, 99.95%), and  $\text{NiO}$  (Cerac, 99%) are dried at appropriate temperatures to remove absorbed moisture.  
 57 Stoichiometric amounts of starting powders are mixed by ball milling for  $\geq 2$  hours in ethanol with yttrium-stabilized  
 58  $\text{ZrO}_2$  grinding media. After evaporation of ethanol, the raw mixtures for samples with  $x = 0.1$  are calcined at  $1073$   
 59  $\text{K}$  for 6 hours in a muffle furnace, while for  $x = 0$  samples,  $873\text{ K}$  for 6 hours is used. The calcined powders are ball  
 60 milled for 12 hours to minimize the particle size and then uniaxially pressed into pellets of 8 mm diameter and 2-4  
 61 mm thickness. In order to minimize the volatilization of K during sintering, all pellet samples are buried in calcined  
 62 powders with the same composition and encapsulated with platinum foil. Pellets are sintered at temperatures which  
 63 depend on compositions, with a dwell time of 1 hour and 5 K/min ramp rate. KNO pellets are sintered at  $1253\text{ K}$  and  
 64  $x = 0.1$  is sintered at  $1418\text{ K}$ . The bulk densities of sintered pellets are calculated through the weights and dimensions  
 65 of the samples; both the  $x = 0$  and  $0.1$  samples show above 92% relative density.

66 Powder X-ray diffraction measurements of sintered ceramics are carried out on a Rigaku GiegerFlex D/Max-B  
 67 diffractometer (40 kV, 30 mA). For dielectric property measurements, sample pellets are first rough polished with 400  
 68 grit polishing paper to obtain parallel top and bottom surfaces. Electrodes are then applied to the pellet by coating  
 69 the polished surfaces with silver paint (Heraeus ST1601-14 type). Platinum lead wires are attached to the surfaces  
 70 using the same silver paint. Paint is dried and sintered at 1023 K for 20 min. to provide a dense electrical contact. The  
 71 dielectric data are collected with a high-precision impedance-capacitance-resistance meter (Hewlett-Packard, model  
 72 4284A) and a high-temperature thermal chamber. The ferroelectric transitions in dense  $(\text{K}_{0.5}\text{Na}_{0.5})\text{NbO}_3$  are used to  
 73 precisely calibrate the temperature (Supplemental Material<sup>62</sup>).

74 Temperature-dependent Raman spectra are collected in the backscattering configuration  $z(x, x + y)\bar{z}$  using a single  
 75 monochromator (XploRA, Horiba Jobin-Yvon, Edison NJ), 4 mW, 532-nm laser excitation, focused through a 10x  
 76 objective to a spot diameter of  $\approx 10 \mu\text{m}$  at an intensity of  $1.6 \times 10^3 \text{ W/cm}^2$ . Light is dispersed using 2400 gr/mm  
 77 gratings and collected using a thermoelectrically cooled array detector. The spectral resolution of this confocal micro-  
 78 Raman instrument under these conditions is  $\approx 1.2 \text{ cm}^{-1}$ . The sample temperature is varied from 83 K to 873 K  
 79 (Linkham THMS 600, instrumental precision  $\pm 0.1 \text{ K}$ ) in increments of 2.5 K (for  $\text{KNbO}_3$ ) and 5 K (for  $\text{KBNNO}$ ) at  
 80 a heating ramp rate of 5 K/min. The sample is also allowed to equilibrate for one minute between consecutive Raman  
 81 scans.

82 We use density functional theory (DFT) calculations to examine the local structure and polarization caused by  
 83 substitution of 0.1  $\text{Ba}(\text{Ni}_{1/2}\text{Nb}_{1/2})\text{O}_{2.75}$  (BNNO) into  $\text{KNO}$ . To directly and accurately model the low concentration  
 84 of Ba and Ni dopant atoms, we use a  $4 \times 4 \times 2$  159-atom supercell, with  $x = 0.125$  BNNO content. This cell contains  
 85 2 Ni atoms and 4 Ba atoms substituting at 2 Nb and 4 K sites. To maintain charge balance, one O atom is removed,  
 86 in two different configurations. For the first configuration, the O vacancy is placed between two Ni atoms located at  
 87 nearest-neighbor  $B$ -sites along the  $z$ -direction, while for the second the vacancy is located between an Nb and an Ni,  
 88 and the two Ni are separated by 7 Å. For computational efficiency, we performed all calculations at the  $\text{KNbO}_3$  lattice  
 89 constants. This choice is supported by the results of the XRD measurements that show that the lattice parameters  
 90 of  $\text{KNbO}_3$  and  $x = 0.1$   $\text{KBNNO}$  are essentially the same. The positions of the ions were fully relaxed at the DFT+ $U$   
 91 level of calculations, using Hubbard  $U$  values of 3.97 eV and 9.9 eV for Nb and Ni, respectively, as in previous  $\text{KBNNO}$   
 92 calculations<sup>10</sup>. Calculations with other values of  $U$  showed only slight dependence of the relaxed structure on the  $U$   
 93 value, supporting the reliability of our choice of  $U$ .

94 The relaxed structures are analyzed for cation displacements which can then be used to evaluate the effect of  
 95 the  $\text{Ba}(\text{Ni,Nb})\text{O}_{2.75}$  substitution on the local structure and to estimate the polarization by multiplying the cation  
 96 displacements by their respective Born effective charge ( $Z^*$ ) values. We also used Berry phase calculations to rigorously  
 97 evaluate the polarization, with good agreement obtained between the approximate displacement-based and the Berry  
 98 phase polarization values. The decomposition of  $P$  into the contributions of individual cation sites enables analysis  
 99 of trends in overall  $P$  in terms of local structure changes.

### 100 III. RESULTS AND DISCUSSION

101 The powder x-ray diffraction results show the formation of a stable perovskite for all compositions, while very small  
 102 NiO impurity peaks are present in samples of  $x = 0.1$  (Figure 1). Dielectric permittivities and losses are obtained  
 103 as a function of temperature and frequency (Figure 2). Samples of composition  $x = 0.1$  show dielectric anomalies  
 104 which indicate phase transitions at 683 K and 533 K. The lack of frequency dependence indicates normal ferroelectric  
 105 behavior, since frequency-dependent dielectric response is characteristic of a relaxor.

106 Since phonon linewidths are temperature-dependent, vibrational mode assignment is most straightforward in low-  
 107 temperature spectra (Figure 3, rhombohedral phase). Neither the  $\text{KNO}$  nor  $\text{KBNNO}$  samples are single-crystalline,  
 108 and therefore the signal measured is an average of many oblique angles not strictly associated with phonon wave vectors  
 109 either parallel or perpendicular to the specific crystallographic axes that would allow for the proper assignment of  
 110 transverse and longitudinal optical (TO, LO) phonon modes<sup>47</sup>. Due to this formalism, the modes will be referred to  
 111 as  $\approx 190 \text{ cm}^{-1}$ ,  $\approx 290 \text{ cm}^{-1}$ ,  $\approx 430 \text{ cm}^{-1}$ ,  $\approx 529 \text{ cm}^{-1}$ ,  $\approx 600 \text{ cm}^{-1}$ , and  $\approx 836 \text{ cm}^{-1}$ ; respectively, for both  $\text{KNO}$  and  
 112  $\text{KBNNO}$  polycrystalline samples with the primarily contributing modes denote in Figure 3. For simplicity, a single  
 113 assignment will follow each mode through softening, stiffening, and any abrupt changes due to structural changes in  
 114 the sample, with the understanding that there are often many modes with overlapping phonon frequency making up  
 115 a spectral feature. Comparable peak energies are observed in the  $\text{KBNNO}$  sample and correspond well to reported  
 116 mode assignments in  $\text{KNbO}_3$ <sup>36,37,48-51</sup>. The  $\text{TO}_1$  mode, associated primarily with ferroelectricity and the polarization  
 117 of the material, corresponds to the central  $B$ -site Nb atoms oscillating against the oxygen octahedra and is shown  
 118 in Figure 4. This mode is particularly indicative of polarization in the material due to the parallel alignment of the  
 119 polarization vector and the Nb-O bond. The  $\text{TO}_2$  mode corresponds to the  $A$ -site K atoms vibrating counter to the  
 120 greater  $\text{NbO}_6$  octahedral structure. The  $\text{TO}_3$  mode corresponds to the  $B$ -site Nb atoms and the apical oxygen atoms

121 moving parallel along the polarization vector, anti-parallel to the equatorial oxygen atoms. The  $A$ -site K atoms do  
 122 not dynamically participate in the  $\text{TO}_3$  mode. The  $\text{TO}_4$  mode corresponds to stationary  $A$  and  $B$ -site atoms and  
 123 apical O atoms, while the equatorial oxygen atoms vibrate out of phase along the polarization direction, with each  
 124 equatorial oxygen atom moving anti-parallel to its nearest equatorial oxygen neighbors.

125 Temperature-dependent Raman spectra for  $\text{KNbO}_3$  (KNO) and  $\text{KBNNNO}$  are shown in Figure 5. Peak fitting analysis  
 126 is performed to quantify the variation of each peak's intensity, width, and position with temperature (Supplemental  
 127 Material<sup>62</sup>). Bose-Einstein correction has been performed before any data analysis of structural phase transitions; in  
 128 addition, the contour plots and stacked plots are normalized for the convenience of the reader, as the low-temperature  
 129 data has much greater signal and lower background than the high-temperature data. Transition temperatures are  
 130 then extracted from the KNO and  $\text{KBNNNO}$  samples based on reported mode assignments, as cited above.

131 Changes in Raman peak positions and intensities are seen at particular temperatures corresponding to first-order  
 132 structural phase transitions: rhombohedral (R)  $\rightarrow$  orthorhombic (O)  $\rightarrow$  tetragonal (T)  $\rightarrow$  cubic (C) (Figure 5).  
 133 While determination of phase transition temperatures can be done by inspection for some modes, detailed analysis  
 134 is required for others (Supplemental Material<sup>62</sup>). For example, the transition temperatures are clear in KNO modes  
 135 of  $\approx 190 \text{ cm}^{-1}$ ,  $\approx 290 \text{ cm}^{-1}$ ,  $\approx 529 \text{ cm}^{-1}$ , and  $\approx 600 \text{ cm}^{-1}$ ; (Figure 5). By contrast, the peaks in the  $\text{KBNNNO}$  solid  
 136 solution sample are much broader, and specific modes (*e.g.* for  $\approx 190 \text{ cm}^{-1}$  and  $\approx 836 \text{ cm}^{-1}$ ) which disappear in  
 137 the end member upon reaching the cubic phase do not disappear at temperatures well above the expected transition  
 138 temperature for the cubic phase in the solid solution. Although the temperature dependence of the relative intensities,  
 139 peak widths, and position are not as distinct as in KNO, the end member's behaviors can be used as a reference for  
 140 mode assignment and to extract the phase transition temperatures for  $\text{KBNNNO}$ .

141 The R  $\rightarrow$  O transition temperature for KNO was established using the relative intensity, mode linewidth, and  
 142 frequency for the  $\approx 190 \text{ cm}^{-1}$ ,  $\approx 290 \text{ cm}^{-1}$ ,  $\approx 430 \text{ cm}^{-1}$ ,  $\approx 529 \text{ cm}^{-1}$ , and  $\approx 600 \text{ cm}^{-1}$  modes (Supplemental Material<sup>62</sup>),  
 143 yielding a R $\rightarrow$ O transition temperature  $T_{\text{R}\rightarrow\text{O}, \text{KNO}}$  of  $272.0 \pm 0.1 \text{ K}$  (Table III). For the  $\text{KBNNNO}$  sample the  $\approx 190$   
 144  $\text{cm}^{-1}$ ,  $\approx 290 \text{ cm}^{-1}$ , and  $\approx 430 \text{ cm}^{-1}$  modes also exhibited abrupt changes, yielding  $T_{\text{R}\rightarrow\text{O}, \text{KBNNNO}} \approx 275 \pm 8 \text{ K}$ . A  
 145 particularly clear example is seen in Figure 6a where the degenerate  $\approx 290 \text{ cm}^{-1}$  modes' frequency undergoes a sharp  
 146 discontinuity which can be clearly observed in the KNO sample. This combination of modes contributing to the  
 147 peak at  $\approx 290 \text{ cm}^{-1}$  softens with higher temperatures. The frequency behavior of the  $\approx 290 \text{ cm}^{-1}$  modes in  $\text{KBNNNO}$   
 148 exhibits a transition and softens, although the mode is much more difficult to resolve due to the various neighboring  
 149 overlapping modes at those temperatures. While the initial frequency discontinuity in the  $\text{KBNNNO}$  sample is more  
 150 subtle, the softening with temperature is much more dramatic for the solid solution when compared to the end  
 151 member.

152 The O  $\rightarrow$  T transition temperature in KNO ( $512 \pm 1 \text{ K}$ ) is determined from the behavior of the  $\approx 190 \text{ cm}^{-1}$ ,  $\approx 290$   
 153  $\text{cm}^{-1}$ ,  $\approx 430 \text{ cm}^{-1}$ ,  $\approx 529 \text{ cm}^{-1}$ , and  $\approx 600 \text{ cm}^{-1}$  modes. The  $\text{KBNNNO}$  transition is ascertained from the  $\approx 430 \text{ cm}^{-1}$ ,  
 154  $\approx 529 \text{ cm}^{-1}$  and  $\approx 600 \text{ cm}^{-1}$  modes with  $T_{\text{O}\rightarrow\text{T}, \text{KBNNNO}}$  of  $523 \pm 6 \text{ K}$ . Determination of this transition temperature in  
 155  $\text{KBNNNO}$  based on other modes, such as the combination of vibrational modes at  $\approx 290 \text{ cm}^{-1}$ , could not be accomplished  
 156 without unacceptably large error. Weighted error analysis is performed using standard expressions for the probability  
 157 distribution and weighting factors (Supplemental Material<sup>62</sup>). This effectively removes the contributions of the  $\approx 290$   
 158  $\text{cm}^{-1}$  modes by weighting them by the inverse of their variance such that they do not significantly affect the  $\text{KBNNNO}$   
 159 transition temperature. Specifically, the  $\approx 430 \text{ cm}^{-1}$  modes are useful for both the KNO and  $\text{KBNNNO}$  samples and  
 160 are significant for determining the O  $\rightarrow$  T transition (Figure 6b).

161 Changes in the mode frequency for  $\approx 430 \text{ cm}^{-1}$  phonons signal the onset of the orthorhombic phase at  $\approx 273 \text{ K}$ . For  
 162 increasing temperature, the modes at  $\approx 430 \text{ cm}^{-1}$  stiffens until the O  $\rightarrow$  T transition occurs, beyond which the modes  
 163 soften slightly until the frequency stabilizes. A decrease in intensity to the background noise level prevents analysis  
 164 at higher temperature. This stiffening and softening behavior around the O  $\rightarrow$  T transition in KNO is used to discern  
 165 the  $\text{KBNNNO}$  transition temperature by identifying the same stiffening and softening in the much broader behavior of  
 166 the  $\approx 430 \text{ cm}^{-1}$  modes. Without the context provided by the response of KNO, assigning the maximum frequency  
 167 of these modes is, at best, challenging considering the various features that affect the relative intensities, linewidths,  
 168 and frequencies of the Raman modes with temperature, including through structural phase transitions<sup>52-55</sup>.

169 The highest-temperature tetragonal to cubic transition, corresponding to the ferroelectric to paraelectric transition,  
 170 in the KNO sample occurs at  $729.2 \pm 0.2 \text{ K}$ , as is most easily seen in the  $\approx 190 \text{ cm}^{-1}$ ,  $\approx 529 \text{ cm}^{-1}$ ,  $\approx 600 \text{ cm}^{-1}$ , and  
 171  $\approx 836 \text{ cm}^{-1}$  modes. At this temperature, the  $\approx 290 \text{ cm}^{-1}$  modes have broadened to the point where the  $\text{TO}_1$  and  
 172  $\text{TO}_4 + \text{LO}_4$  contributions are indistinguishable. Additionally, the modes at  $\approx 290 \text{ cm}^{-1}$  and  $\approx 430 \text{ cm}^{-1}$  that give  
 173 signal above the background at lower temperatures have decreased or vanished as expected from previous studies of  
 174 the mode evolution in  $\text{KNO}$ <sup>36,37,48-51</sup>. The  $\approx 190 \text{ cm}^{-1}$ ,  $\approx 529 \text{ cm}^{-1}$ , and  $\approx 600 \text{ cm}^{-1}$  modes in the Raman spectra  
 175 for the  $\text{KBNNNO}$  sample yield  $T_{\text{T}\rightarrow\text{C}, \text{KBNNNO}} \approx 736 \pm 7 \text{ K}$ . Through this transition temperature, the  $\approx 600 \text{ cm}^{-1}$  mode  
 176 condenses into the  $\approx 529 \text{ cm}^{-1}$  mode to become a single mode at high temperatures<sup>38</sup> for both KNO and  $\text{KBNNNO}$   
 177 (Figure 5). The temperature dependence of the Raman mode frequency for the  $\approx 529 \text{ cm}^{-1}$  mode can be traced until  
 178 it becomes indistinguishable with the  $\approx 600 \text{ cm}^{-1}$  mode (Figure 7a). As expected with  $\approx 529 \text{ cm}^{-1}$ , there is a general

179 softening through the rhombohedral, orthorhombic, and tetragonal phases and transitions and significant changes to  
 180 the mode linewidth through the various transitions as well (Figure 7b). Coalescing of  $\approx 529 \text{ cm}^{-1}$  and  $\approx 600 \text{ cm}^{-1}$   
 181 to degeneracy near  $\approx 560 \text{ cm}^{-1}$  is most clearly seen in Figure 7c. The amplitude of  $\approx 600 \text{ cm}^{-1}$  in KNO is seen to  
 182 increase discontinuously at the transition temperature we assign to the merging of this mode with the  $\approx 529 \text{ cm}^{-1}$ .  
 183 This justifies allowing the fitted amplitude of  $\approx 600 \text{ cm}^{-1}$  to decrease to zero as the two modes become degenerate  
 184 (Supplemental Material)<sup>52,54,62</sup>.

185 DFT calculations are performed for cation configurations where the vacancy is located between two Ni atoms and  
 186 also where the vacancy is located between Ni and Nb atoms, with another Ni surrounded by 6 O atoms. We find that  
 187 the configuration with the vacancy between the two Ni is lower in energy by 1.48 eV. Such a large energy difference  
 188 suggests that KBNNO will mostly contain Ni-O<sub>vac</sub>-Ni configurations.

189 In a  $4 \times 4 \times 2$  supercell,  $x$  and  $y$  are the long directions and  $z$  is the short direction. We place the two Ni along the  $x$   
 190 direction and relax all ions starting with the cations displaced along  $\langle 111 \rangle$ . Berry phase polarization calculations for  
 191 the relaxed structure indicate that the values of the polarization components in the  $x$ ,  $y$  and  $z$  directions are 0.142  
 192 C/m<sup>2</sup>, 0.192 and 0.208 C/m<sup>2</sup>, respectively. The polarization values in the  $y$  and  $z$  directions are slightly smaller than  
 193 the 0.233 C/m<sup>2</sup> obtained for the  $x$ ,  $y$  and  $z$   $P$  components of the KNbO<sub>3</sub> parent material in the 0 K rhombohedral  
 194 phase. The polarization component along the  $x$  direction is more significantly reduced to 0.142 C/m<sup>2</sup>. Examination  
 195 of the local displacements shows that the introduction of BNNO leads to a distribution of the local Nb displacements,  
 196 with Nb off-centering magnitudes in a given Cartesian direction varying from 0 to 0.135 Å with the average Nb  
 197 displacement magnitude of 0.16 Å. These average displacement values are smaller than the 0.103 Å displacements  
 198 along the  $x$ ,  $y$  and  $z$  direction found for KNbO<sub>3</sub> by our DFT calculations.

199 Using a previously established correlation between the experimentally observed  $T_c$  and the square of the 0 K DFT  
 200 polarization<sup>56–60</sup>, we estimate a decreased  $T_c$  for KBNNO of either  $\approx 433$  K based on the average total  $P$ , or  $\approx 573$  K  
 201 based on the average magnitude of the Nb displacements related to the local polarization. While also predicting  
 202 a stable room-temperature ferroelectricity in KBNNO, these values underestimate both the dielectric tetragonal to  
 203 cubic (T-C) transition temperature of 683 K as well as the 736 K T-C transition temperature extracted from the  
 204 Raman results. This discrepancy could be ascribed to the somewhat qualitative nature of the correlation between  
 205  $T_c$  and  $P^2$  for materials with different local structures. The presence of Ni + O<sub>vac</sub> introduces structural motifs into  
 206 KBNNO that are entirely absent in KNO, diminishing the predictive accuracy of the  $T_c - P^2$  correlation.

207 The DFT finding of a distribution of Nb displacement magnitudes and variation in the local structure is consistent  
 208 with broadening in both the dielectric and Raman data, including the Raman linewidth. In particular, the temperature  
 209 evolution of the Raman shift used to assign the T-C transition temperature changes from an abrupt drop at  $T_c$  observed  
 210 for KNO to a gradual decrease to a constant value observed for KBNNO. It is likely that the distribution of local  
 211 environments found in KBNNO leads to a broader distribution of Raman shifts, with the local environments displaying  
 212 enhanced (relative to KNO) Nb displacements accounting for the higher temperature plateauing of the Raman shift  
 213 that signifies the presence of the T-C transition. Such dependence of the Raman shift on the distribution of local  
 214 structures (*i.e.* on the strong displacement contributions) is perhaps the explanation for the disagreement between  
 215 the enhanced  $T_c$  found by Raman results and the decreased  $T_c$  found by the dielectric measurements. The dielectric  
 216 results are given by the average structure of the material, where a decrease in the displacement and  $P$  is observed for  
 217 KBNNO, corresponding to a less stable  $P$  and a lower FE-PE transition temperature. On the other hand, the Raman  
 218 measurements are sensitive to the variation in the local structure, where some local environments exhibit enhanced  
 219 0 K displacements that are likely to persist to higher temperature than the FE structure in the parent KNO material.

220

#### IV. CONCLUSIONS

221 Dielectric permittivity measurements and Raman spectroscopy are used to probe temperature-dependent structural  
 222 and ferroelectric phase evolution. Changes in the temperature-dependent Raman shifts are diffuse in KBNNO as com-  
 223 pared with abrupt transitions observed in the end member KNO. Taken together with variations in DFT-calculated  
 224 local atom displacements and local and averaged polarizations (the extent of applicability of  $T_c - P^2$  scaling notwith-  
 225 standing), and the absence of frequency dispersion in the dielectric permittivity, these results indicate persistence of  
 226 ferroelectric ordering in KBNNO to temperatures that approach the  $T_c$  of the end member KNbO<sub>3</sub>. This identifica-  
 227 tion of structural and ferroelectric phases, combined with the ability to tune these solid-solution ceramic materials  
 228 compositionally, highlights these oxides' promising application as semiconducting ferroelectric absorbers and carrier  
 229 separating layers in novel photovoltaic devices.

## ACKNOWLEDGMENTS

231 Work at Drexel supported by the US Army Research Office (ARO) under grant no. W911NF-14-1-0500 and the  
 232 National Science Foundation (NSF) under grant numbers DMR 1608887 and DMR 1124696. Theoretical work was  
 233 supported by the Department of Energy Office of Basic Energy Sciences, under grant DE-FG02-07ER46431. The  
 234 authors acknowledge the use of the Core Facilities at Drexel University and Raman instrumentation acquisition via  
 235 the ARO Defense University Research Instrumentation Program (DURIP). The authors acknowledge computational  
 236 support from the National Energy Research Scientific Computing Center of the Department of Energy.

---

237 \* jes53@drexel.edu

- 238 <sup>1</sup> S. Y. Yang, J. Seidel, S. J. Byrnes, P. Shafer, C. H. Yang, M. D. Rossell, P. Yu, Y. H. Chu, J. F. Scott, J. W. Ager, L. W.  
 239 Martin, and R. Ramesh, *Nat. Nanotechnol.* **5**, 143 (2010).  
 240 <sup>2</sup> J. Seidel, D. Fu, S.-Y. Yang, E. Alarcón-Lladó, J. Wu, R. Ramesh, and J. W. Ager, *Phys. Rev. Lett.* **107**, 126805 (2011).  
 241 <sup>3</sup> M. Alexe and D. Hesse, *Nat. Commun.* **2**, 256 (2011).  
 242 <sup>4</sup> R. Nechache, C. Harnagea, S. Licoccia, E. Traversa, A. Ruediger, A. Pignolet, and F. Rosei, *Appl. Phys. Lett.* **98**, 202902  
 243 (2011).  
 244 <sup>5</sup> S. M. Young and A. M. Rappe, *Phys. Rev. Lett.* **109**, 116601 (2012).  
 245 <sup>6</sup> S. M. Young, F. Zheng, and A. M. Rappe, *Phys. Rev. Lett.* **109**, 236601 (2012).  
 246 <sup>7</sup> J. Kreisel, M. Alexe, and P. A. Thomas, *Nat. Mater.* **11**, 260 (2012).  
 247 <sup>8</sup> D. Daranciang, M. J. Highland, H. Wen, S. M. Young, N. C. Brandt, H. Y. Hwang, M. Vattilana, M. Nicoul, F. Quirin,  
 248 J. Goodfellow, T. Qi, I. Grinberg, D. M. Fritz, M. Cammarata, D. Zhu, H. T. Lemke, D. A. Walko, E. M. Dufresne, Y. Li,  
 249 J. Larsson, D. A. Reis, K. Sokolowski-Tinten, K. A. Nelson, A. M. Rappe, P. H. Fuoss, G. B. Stephenson, and A. M.  
 250 Lindenberg, *Phys. Rev. Lett.* **108**, 087601 (2012).  
 251 <sup>9</sup> B. Yang, Y. Yuan, P. Sharma, S. Poddar, R. Korlacki, S. Ducharme, A. Gruverman, R. Saraf, and J. Huang, *Adv. Mater.*  
 252 **24**, 1455 (2012).  
 253 <sup>10</sup> I. Grinberg, D. V. West, M. Torres, G. Gou, D. M. Stein, L. Wu, G. Chen, E. M. Gallo, A. R. Akbashev, P. K. Davies, J. E.  
 254 Spanier, and A. M. Rappe, *Nature* **503**, 509 (2013).  
 255 <sup>11</sup> V. Fridkin, *IEEE Trans. Sonics Ultrason.* **60**, 1551 (2013).  
 256 <sup>12</sup> A. Bhatnagar, A. Roy Chaudhuri, Y. Heon Kim, D. Hesse, and M. Alexe, *Nat. Commun.* **4** (2013).  
 257 <sup>13</sup> Z. Xiao, Q. Dong, P. Sharma, Y. Yuan, B. Mao, W. Tian, A. Gruverman, and J. Huang, *Adv. Energy Mater.* **3**, 1672  
 258 (2013).  
 259 <sup>14</sup> R. Nechache, C. Harnagea, S. Li, L. Cardenas, W. Huang, J. Chakrabartty, and F. Rosei, *Nat. Photonics* **9**, 61 (2015).  
 260 <sup>15</sup> A. Zenkevich, Y. Matveyev, K. Maksimova, R. Gaynudinov, A. Tolstikhina, and V. Fridkin, *Phys. Rev. B* **90**, 161409  
 261 (2014).  
 262 <sup>16</sup> Y. Yuan, Z. Xiao, B. Yang, and J. Huang, *J. Mater. Chem. A* **2**, 6027 (2014).  
 263 <sup>17</sup> J. P. Chakrabartty, R. Nechache, C. Harnagea, and F. Rosei, *Opt. Express* **22**, A80 (2014).  
 264 <sup>18</sup> J. E. Spanier, V. M. Fridkin, A. M. Rappe, A. R. Akbashev, A. Polemi, Y. Qi, Z. Gu, S. M. Young, C. J. Hawley, D. Imbrenda,  
 265 G. Xiao, A. L. Bennett-Jackson, and C. L. Johnson, *Nat. Photonics* **10**, 611 (2016).  
 266 <sup>19</sup> A. A. Grekov, M. A. Malitskaya, V. D. Spitsina, and V. M. Fridkin, *Kristallografiya* **15**, 500 (1970).  
 267 <sup>20</sup> A. M. Glass, D. von der Linde, and T. J. Negran, *Appl. Phys. Lett.* **25**, 233 (1974).  
 268 <sup>21</sup> V. Belincher and B. Sturman, *Phys.-Usp.* **23**, 199 (1980).  
 269 <sup>22</sup> B. Sturman and V. Fridkin, *The photovoltaic and photorefractive effects in noncentrosymmetric materials* (Gordon and  
 270 Breach, Philadelphia, 1992).  
 271 <sup>23</sup> J. W. Bennett, I. Grinberg, and A. M. Rappe, *J. Am. Chem. Soc.* **130**, 17409 (2008).  
 272 <sup>24</sup> G. Y. Gou, J. W. Bennett, H. Takenaka, and A. M. Rappe, *Phys. Rev. B* **83**, 205115 (2011).  
 273 <sup>25</sup> T. Qi, I. Grinberg, and A. M. Rappe, *Phys. Rev. B* **83**, 224108 (2011).  
 274 <sup>26</sup> F. Wang, I. Grinberg, L. Jiang, S. M. Young, P. K. Davies, and A. M. Rappe, *Ferroelectrics* **483**, 1 (2015).  
 275 <sup>27</sup> F. Wang, S. M. Young, F. Zheng, I. Grinberg, and A. M. Rappe, *Nat. Commun.* **7**, 10419 (2016).  
 276 <sup>28</sup> F. Wang and A. M. Rappe, *Phys. Rev. B* **91**, 165124 (2015).  
 277 <sup>29</sup> W. Zhou, H. Deng, P. Yang, and J. Chu, *Appl. Phys. Lett.* **105**, 111904 (2014).  
 278 <sup>30</sup> G. H. Haertling and C. E. Land, *J. Am. Ceram. Soc.* **54**, 1 (1971).  
 279 <sup>31</sup> L. Davis and L. G. Rubin, *J. Appl. Phys.* **24**, 1194 (1953).  
 280 <sup>32</sup> B. T. Matthias and J. P. Remeika, *Phys. Rev.* **82**, 727 (1951).  
 281 <sup>33</sup> G. Shirane, R. Newnham, and R. Pepinsky, *Phys. Rev.* **96**, 581 (1954).  
 282 <sup>34</sup> M. Fontana and C. Razzetti, *Solid State Commun.* **17**, 377 (1975).  
 283 <sup>35</sup> J. Hurrell and D. Bozini, *Solid State Commun.* **17**, 1541 (1975).  
 284 <sup>36</sup> M. D. Fontana, G. Dolling, G. E. Kugel, and C. Carabatos, *Phys. Rev. B* **20**, 3850 (1979).  
 285 <sup>37</sup> M. D. Fontana, G. E. Kugel, G. Metrat, and C. Carabatos, *Phys. Status Solidi B* **103**, 211 (1981).  
 286 <sup>38</sup> M. D. Fontana, G. Metrat, J. L. Servoin, and F. Gervais, *J. Phys. C: Solid State Phys.* **17**, 483 (1984).

- 287 <sup>39</sup> M. D. Fontana, A. Ridah, G. E. Kugel, and C. Carabatos-Nedelec, *J. Phys. C: Solid State Phys.* **21**, 5853 (1988).
- 288 <sup>40</sup> R. Currat, H. Buhay, C. H. Perry, and A. M. Quittet, *Phys. Rev. B* **40**, 10741 (1989).
- 289 <sup>41</sup> E. Buixaderas, D. Nuzhnyy, I. Gregora, S. Kamba, M. Berta, B. Malic, and M. Kosec, *IEEE Trans. Sonics Ultrason.* **56**,  
290 1843 (2009).
- 291 <sup>42</sup> N. Klein, E. Hollenstein, D. Damjanovic, H. J. Trodahl, N. Setter, and M. Kuball, *J. Appl. Phys.* **102**, 014112 (2007).
- 292 <sup>43</sup> A. Bartasyte, J. Kreisel, W. Peng, and M. Guilloux-Viry, *Appl. Phys. Lett.* **96**, 262903 (2010).
- 293 <sup>44</sup> L. Luisman, A. Feteira, and K. Reichmann, *Appl. Phys. Lett.* **99**, 192901 (2011).
- 294 <sup>45</sup> H. J. Trodahl, N. Klein, D. Damjanovic, N. Setter, B. Ludbrook, D. Rytz, and M. Kuball, *Appl. Phys. Lett.* **93**, 262901  
295 (2008).
- 296 <sup>46</sup> I. S. Golovina, V. P. Bryksa, V. V. Strelchuk, I. N. Geifman, and A. A. Andriiko, *J. Appl. Phys.* **113**, 144103 (2013).
- 297 <sup>47</sup> R. Loudon, *Advances in Physics* **13**, 423 (1964).
- 298 <sup>48</sup> G. E. Kugel, M. D. Fontana, J. Vamvakas, and C. Carabatos, “Raman spectroscopy, linear and nonlinear: proceedings of  
299 the eighth international Conference on Raman Spectroscopy, Bordeaux, France, 6-11 September,” (John Wiley and sons,  
300 1982) p. 457.
- 301 <sup>49</sup> A. M. Quittet, J. L. Servoin, and F. Gervais, *J. Phys. France* **42**, 493 (1981).
- 302 <sup>50</sup> D. G. Bozinis and J. P. Hurrell, *Phys. Rev. B* **13**, 3109 (1976).
- 303 <sup>51</sup> A. V. Postnikov, T. Neumann, and G. Borstel, *Phys. Rev. B* **50**, 758 (1994).
- 304 <sup>52</sup> A. M. Quittet, M. I. Bell, M. Krauzman, and P. M. Raccah, *Phys. Rev. B* **14**, 5068 (1976).
- 305 <sup>53</sup> L. H. Robins, D. L. Kaiser, L. D. Rotter, P. K. Schenck, G. T. Stauf, and D. Rytz, *J. Appl. Phys.* **76**, 7487 (1994).
- 306 <sup>54</sup> G. E. Kugel, M. D. Fontana, J. Vamvakas, and C. Carabatos, *Ferroelectrics* **55**, 27 (1984).
- 307 <sup>55</sup> M. Fontana, G. Kugel, J. Vamvakas, and C. Carabatos, *Solid State Commun.* **45**, 873 (1983).
- 308 <sup>56</sup> S. C. Abrahams, S. K. Kurtz, and P. B. Jamieson, *Phys. Rev.* **172**, 551 (1968).
- 309 <sup>57</sup> I. Grinberg and A. M. Rappe, *Phys. Rev. B* **70**, 220101 (2004).
- 310 <sup>58</sup> I. Grinberg and A. M. Rappe, *Phys. Rev. Lett.* **98**, 037603 (2007).
- 311 <sup>59</sup> J. Chen, K. Nittalla, J. L. Jones, P. Hu, and X. Xing, *Appl. Phys. Lett.* **96**, 252908 (2010).
- 312 <sup>60</sup> A. Berenov, F. L. Goupil, and N. Alford, *Sci. Rep.* **6**, 28055 (2016).
- 313 <sup>61</sup> A. V. Postnikov and G. Borstel, *Phys. Rev. B* **50**, 16403 (1994).
- 314 <sup>62</sup> See Supplemental Material [url] for description of analysis, additional synthesis details, X-ray diffraction measurements, and  
315 additional dielectric constant and loss measurements which includes Refs. 52,54,63–71.
- 316 <sup>63</sup> *IGOR Pro*, version 6.0 ed. (WaveMetrics, Inc., Lake Oswego, OR, 2008).
- 317 <sup>64</sup> W. H. Press, S. A. Teukolsky, W. T. Vetterling, and B. P. Flannery, *Numerical Recipes in C (2nd Ed.): The Art of Scientific  
318 Computing* (Cambridge University Press, New York, NY, USA, 1992).
- 319 <sup>65</sup> A. G. Palmer III, M. Rance, and P. E. Wright, *J. Am. Ceram. Soc.* **113**, 4371 (1991).
- 320 <sup>66</sup> D. J. Hudson, *J. Am. Stat. Assoc.* **61**, 1097 (1966).
- 321 <sup>67</sup> A. Ganse, Multi-Phase Linear Regression, <https://github.com/aganse/MultiRegressLines.matlab>, Downloaded on December  
322 1, 2015. Line 96 was edited to correct a sum of residuals squared error.
- 323 <sup>68</sup> G. Holton, *Value-at-Risk: Theory and Practice* (Academic Press, San Diego, CA, USA, 2003).
- 324 <sup>69</sup> P. R. Renne, A. L. Deino, R. C. Walter, B. D. Turrin, C. C. Swisher, III, T. A. Becker, G. H. Curtis, W. D. Sharp, and  
325 A.-R. Jaouni, *Geology* **22**, 783 (1994).
- 326 <sup>70</sup> I. Kirsch, B. J. Deacon, T. B. Huedo-Medina, A. Scoboria, T. J. Moore, and B. T. Johnson, *PLOS Medicine* **5**, 1 (2008).
- 327 <sup>71</sup> J.-F. Li, K. Wang, F.-Y. Zhu, L.-Q. Cheng, and F.-Z. Yao, *J. Am. Ceram. Soc.* **96**, 3677 (2013).



TABLE I. Twelve optical phonon modes of KNO, as predicted by Postnikov *et al.*<sup>61</sup> for the room temperature orthorhombic phase. Included are experimental values from this study.

Mode	Symm.	Calculated Frequency (cm <sup>-1</sup> )	Experimental Values (cm <sup>-1</sup> )
	B <sub>2</sub>	soft	
TO <sub>1</sub>	B <sub>1</sub>	232	250
	A <sub>1</sub>	257	296
TO <sub>2</sub>	B <sub>2</sub>	185	192
	B <sub>1</sub>	146	a
	A <sub>1</sub>	186	275
TO <sub>3</sub>	B <sub>2</sub>	467	532
	B <sub>1</sub>	528	b
	A <sub>1</sub>	593	596
TO <sub>4</sub>	B <sub>1</sub>	297	c
	A <sub>1</sub>	307	c
	A <sub>2</sub>	224	c

<sup>a</sup> indistinguishable with B<sub>2</sub>(TO<sub>2</sub>)

<sup>b</sup> indistinguishable with B<sub>2</sub>(TO<sub>3</sub>)

<sup>c</sup> indistinguishable with A<sub>1</sub>(TO<sub>1</sub>)

TABLE II. Summary of optical modes associated with the four structural phases in KNO and KBNNO.

Phase	Space Group	Point Group	Optical Modes
Rhombohedral	<i>R3m</i>	<i>C</i> <sub>3v</sub> <sup>5</sup>	3 A <sub>1</sub> (T <sub>z</sub> , α <sub>xx</sub> + α <sub>yy</sub> , α <sub>zz</sub> ) + A <sub>2</sub> <sup>*</sup> + 4 E (T <sub>x</sub> , T <sub>y</sub> , α <sub>xx</sub> - α <sub>yy</sub> , α <sub>xy</sub> , α <sub>xz</sub> , α <sub>yz</sub> )
Orthorhombic	<i>Amm2</i>	<i>C</i> <sub>4v</sub> <sup>14</sup>	4 A <sub>1</sub> (T <sub>z</sub> , α <sub>xx</sub> , α <sub>yy</sub> , α <sub>zz</sub> ) + A <sub>2</sub> (α <sub>xy</sub> ) + 4 B <sub>1</sub> (T <sub>x</sub> , α <sub>xz</sub> ) + 3 B <sub>2</sub> (T <sub>y</sub> , α <sub>yz</sub> )
Tetragonal	<i>P4mm</i>	<i>C</i> <sub>4v</sub> <sup>1</sup>	3 A <sub>1</sub> (T <sub>z</sub> , α <sub>xx</sub> + α <sub>yy</sub> , α <sub>zz</sub> ) + B <sub>1</sub> (α <sub>xx</sub> - α <sub>yy</sub> ) + 4 E(T <sub>x</sub> , T <sub>y</sub> , α <sub>xz</sub> , α <sub>yz</sub> )
Cubic	<i>Pm3m</i>	<i>O</i> <sub>h</sub> <sup>1</sup>	3 F <sub>1u</sub> <sup>*</sup> (T <sub>x</sub> , T <sub>y</sub> , T <sub>z</sub> ) + F <sub>2u</sub> <sup>*</sup>

\* mode is not Raman active

TABLE III. Summary of structural phase transition temperatures as determined from Raman.

	Rhombohedral → Orthorhombic (R→O)	Orthorhombic → Tetragonal (O→T)	Tetragonal → Cubic (T→C)
KNO	272.0±0.1 K	512±1 K	729.2±0.2 K
KBNNO	275±8 K	523±6 K	736±7 K

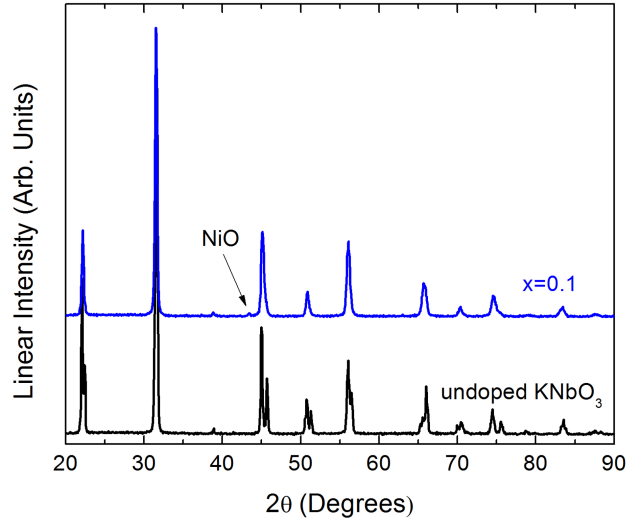


FIG. 1. X-ray diffraction spectra of end member KNO and  $x = 0.1$  KBNNO stoichiometry. Arrows indicate the inclusion of NiO. Additional stoichiometries available in Supplemental Material<sup>62</sup>.

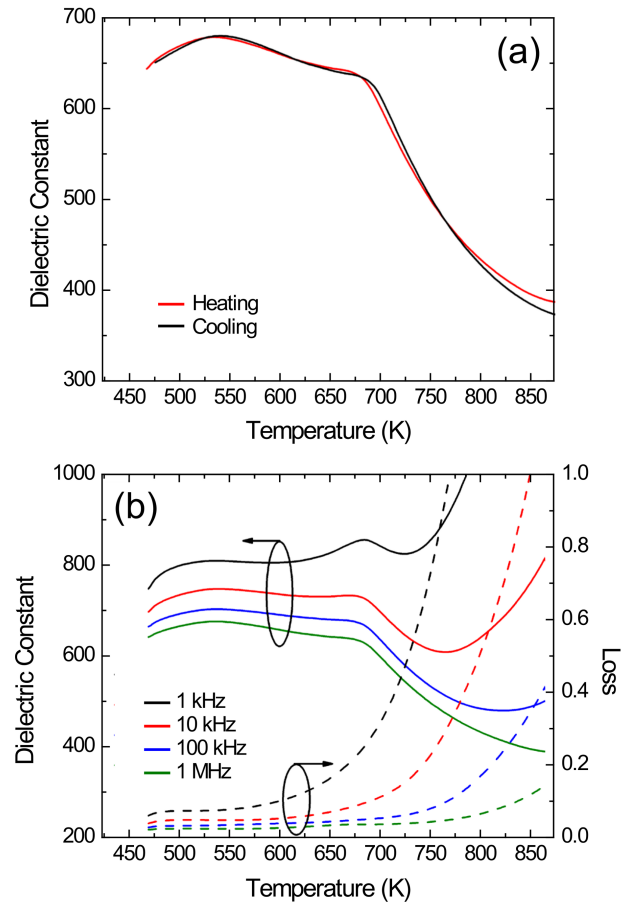


FIG. 2. Temperature dependence of dielectric permittivity measured at 1 MHz for (a) KBNNO  $x = 0.1$ ; heating cycle and cooling cycle are red and black respectively. (b) Temperature-dependent dielectric permittivity and loss of KBNNO  $x = 0.1$  for various  $E$ -field frequencies.

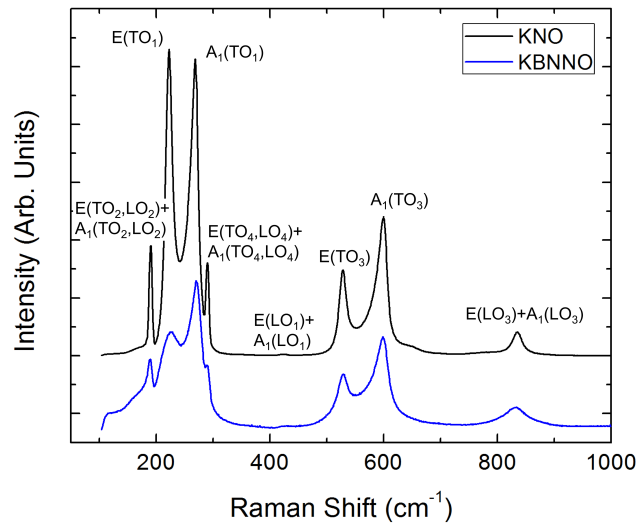


FIG. 3. Raman spectra of the KNO and KBNNO samples in the rhombohedral phase collected at 83 K with approximate mode assignments from bulk and polycrystalline literature showing overall agreement between end member KNO and solid-solution KBNNO<sup>36,37,48–51</sup>.

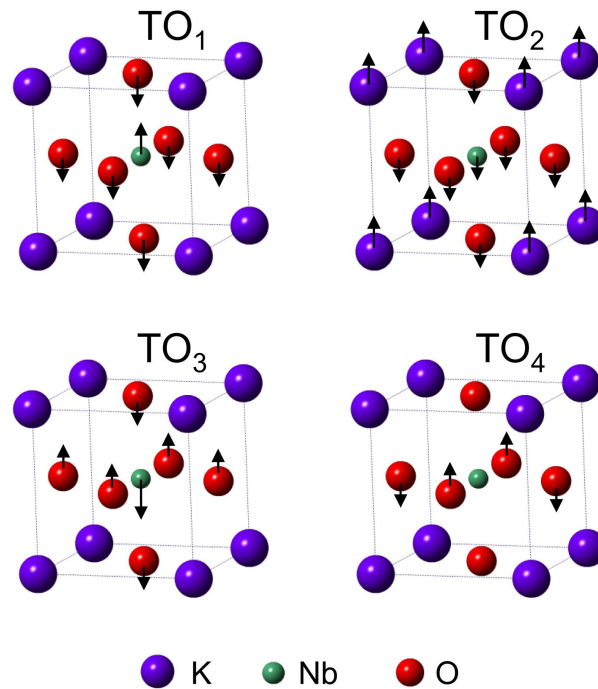


FIG. 4. Ionic displacements associated with the four transverse optical phonons from lattice dynamics calculations<sup>37</sup>.

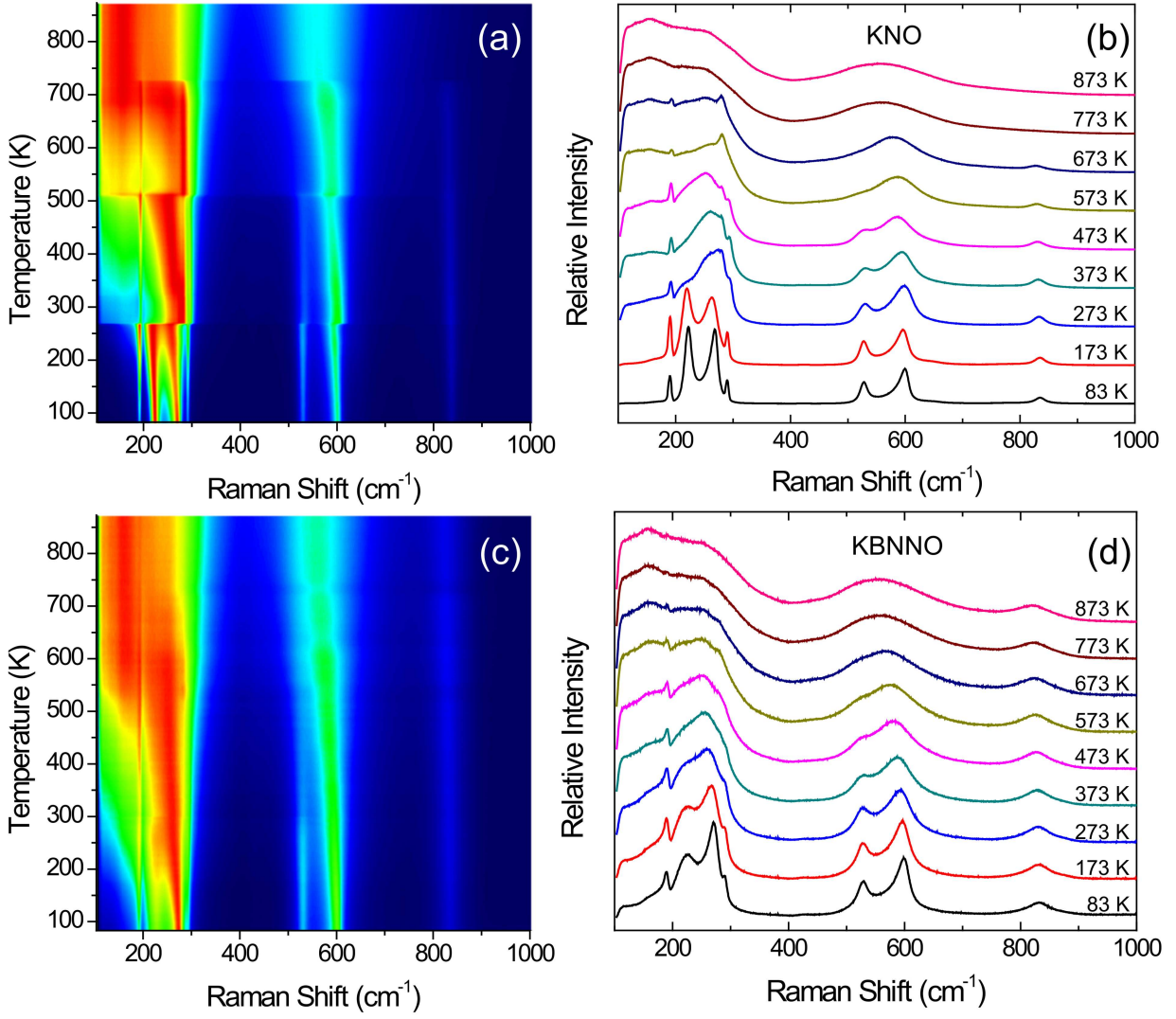


FIG. 5. Raman scattering spectra of KNO ceramic materials as a color map (a) and at selected temperatures (b). Raman spectra of KBNNO ceramic materials is shown as a color map (c) and at selected temperatures (d). Phase transitions more evident in KNO, but both ceramics show spectral characteristics revealing  $R \rightarrow O \rightarrow T \rightarrow C$  phase transitions.

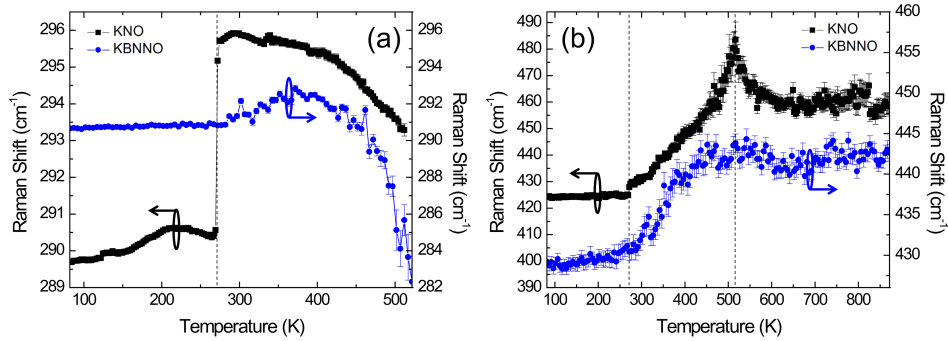


FIG. 6. (a) Temperature dependence of the overlapping phonon modes near  $290 \text{ cm}^{-1}$ . While a  $>4 \text{ cm}^{-1}$  increase in peak energy is seen for KNO, signaling the  $R \rightarrow O$  transition, a much smaller change is observed for KBNNO, as confirmed by analysis of the  $\approx 430 \text{ cm}^{-1}$  mode. (b) Temperature dependence of the  $\approx 430 \text{ cm}^{-1}$  modes shows a maximum stiffening which signals the  $O \rightarrow T$  phase transition in KNO; a broader, weaker maximum is also seen at the same temperature in KBNNO. Vertical dashed lines correspond to determined phase transition temperatures in KNO.

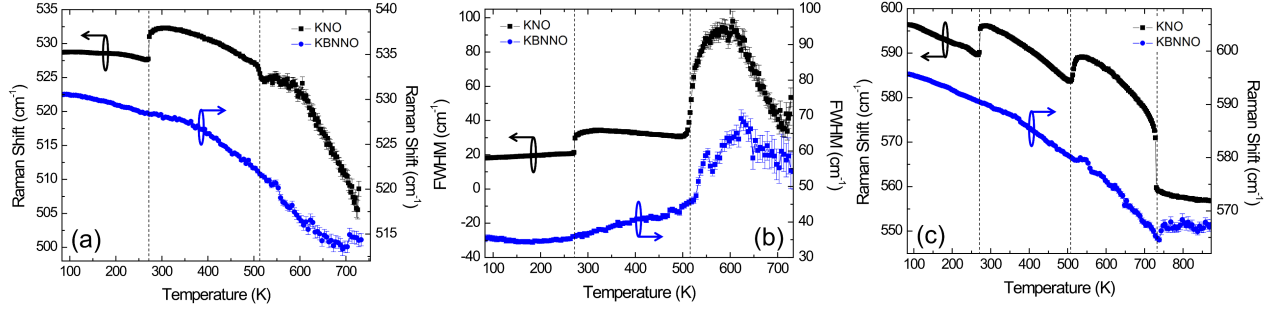


FIG. 7. Comparison of the fitted temperature dependences of the  $\approx 529 \text{ cm}^{-1}$  and  $\approx 600 \text{ cm}^{-1}$  modes (a) energy and (b) linewidth in KNO and KBNNO, enabling extraction of the O  $\rightarrow$  T transition temperature; the  $\approx 529 \text{ cm}^{-1}$  modes become degenerate with the  $\approx 600 \text{ cm}^{-1}$  in the cubic phase and is only shown in (c). (c) Comparison of the  $\approx 600 \text{ cm}^{-1}$  mode softening in KNO and KBNNO. The behavior of the KNO and KBNNO modes here is qualitatively similar and, upon phase transition, the  $\approx 600 \text{ cm}^{-1}$  becomes degenerate with the  $\approx 529 \text{ cm}^{-1}$  modes to collect around  $560 \text{ cm}^{-1}$  enabling determination of T  $\rightarrow$  C transition temperatures.